Supplementary Material: "Effects of altermagnetic order, strain and doping in RuO_2"

Darshana Wickramaratne,* Marc Currie, Shelby S. Fields, Cory D. Cress, and Steven P. Bennett
US Naval Research Laboratory, Washington, D.C. 20375, USA
(Dated: November 10, 2025)

I. SHIFT IN THE XRD PEAK POSITIONS FOR RUO_2 GROWN ON DIFFERENT SUBSTRATES

Orientation	Peak	Experimental Position, 2θ (°)	Experimental Spacing (Å)	Bulk Spacing (Å)
(001)	002	59.67	1.55	1.5655
(110)	110	27.92	3.19	3.19
	220	57.65	1.60	1.59
	330	92.63	1.07	1.06
(101)	101	35.43	2.53	2.57
	202	74.77	1.27	1.29

TABLE S1. Comparison of XRD peak positions for RuO_2 on TiO_2

II. IMPACT OF LATTICE PARAMETERS ON THE CALCULATED VIBRATIONAL FREQUENCIES

The calculated lattice parameters in the NM state are larger than the experimental parameters by up to 0.5% (consistent with the tendency for the GGA functional to overestimate lattice parameters) while the in-plane lattice parameter in the AM state is 1% larger than experiment while the out-of-plane lattice parameter is 1% lower than the experimental value. To determine to what degree the lattice parameters affect the calculated vibrational frequencies we calculated the Raman frequencies in the NM state and AM state using the bulk experimental lattice parameters (listed in Table I of the main text). The calculated frequencies are listed below. In the NM state the frequency of

	NM	AM
B_{2g}	87 (88)	88 (90)
A_{1g}	78 (78)	82 (84)
E_g	62 (63)	66 (67)
B_{1g}	21 (20)	20 (19)

TABLE S2. First-principles calculations of the Raman frequencies (listed in meV) in the NM and the AM state using the experimental lattice parameters of bulk RuO_2. The Raman frequencies that were calculated using the equilibrium lattice parameters of the relaxed structures (listed in Table I of the main text) are included in brackets.

the B_{2g} and B_{1g} modes differ by 1 meV from the corresponding value in the main text (which use the GGA lattice parameters) In the AM state, the Raman frequencies obtained with the experimental lattice parameters are lower than the frequencies obtained using the equilibrium calculated lattice parameters in the AM state, which is likely due to the slightly larger volume of the unitcell based on the experimental lattice parameters.

* darshana.k.wickramaratne.civ@us.navy.mil

III. FITTING ELLIPSOMETRY DATA

To analyze the ellipsometry data two models were created. Each model has a Drude term and three oscillator terms. The first model uses three Lorentzian oscillators, and the second uses three Gaussians. Since we found the Gaussian oscillator model yielded better fits to our experimental data we only present the details for the Gaussian oscillator model. We also considered an additional model that minimized the optical constants on a per point basis, with each beginning with the results of one of the two oscillator models. The results for both yielded near identical results. The model with the Drude term and three Gaussian oscillators is defined as follows

$$\varepsilon = 1 + \frac{A_1 B_1}{E^2 - iB_1 E} + \sum_{n=2}^{4} \varepsilon_n^{\text{Gauss}}(E_n, A_n, B_n)$$

where $\varepsilon_n^{\text{Gauss}} = \varepsilon_n' + i\varepsilon_n''$ and $\varepsilon_n'' = \frac{A_n}{B_n} \cdot e^{-\left(\frac{E-E_n}{\sigma}\right)^2} - \frac{A_n}{B_n} \cdot e^{-\left(\frac{E+E_n}{\sigma}\right)^2}$. We apply Kramers-Kronig integration as follows $\varepsilon' = \frac{2}{\pi} \cdot P \int_0^\infty \frac{\xi \varepsilon''(\xi)}{\xi^2 - E^2}\, d\xi$ to obtain the real part. The broadening σ, that applies to the imaginary component of the Gaussian oscillator is defined as $\sigma = \frac{B_n}{2\sqrt{\ln(2)}}$. Based on our fitting we obtain the following parameters to the model

n	E (eV)	A_n	B_n
1	-	33.9	0.77
2	2.60	2.03	0.73
3	3.28	4.50	1.21
4	5.71	17.1	3.07

TABLE S3. Parameters used within the Gaussian oscillator model to fit to the experimental ellipsometry data.

In Fig. S1 we compare the measured real component of the refractive index, n, and the imaginary component of the refractive index, k obtained from our ellipsometry measurements of RuO_2 on TiO_2 (001).

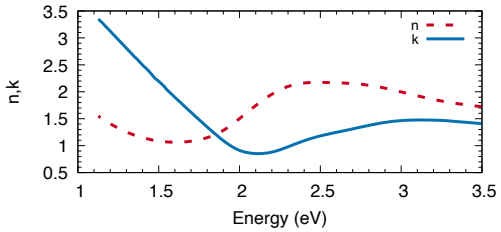

FIG. S1. Real component of the refractive index, n (red dotted line) and the imaginary component of the refractive index, k (blue solid line).

IV. RAMAN SCATTERING, TRANSMITTANCE AND REFLECTIVITY MEASUREMENTS OF RuO_2 ON TiO_2

We use two excitation wavelengths for our Raman measurements, 532 nm and 455 nm. For the samples excited with a 532 nm wavelength source, the excitation power level was <1.2 mW and the beam was focused to <1 μm diameter on the surface of the sample, which leads to a peak irradiance < 200 kW/cm^2. For the 455 nm source we used a excitation power level of 5 mW. Confocal images and the corresponding Raman maps were collected with 455 nm excitation. over areas of approximately 8 mm by 10 mm with a step size of 0.3 mm leading to about 900 spectra per mapped region. For peak analysis, spectra were averaged over the entire mapped region.

The frequencies of the Raman active modes obtained from fitting our measurements of RuO_2 grown on the different TiO_2 substrates is listed in Table S4. The frequency of the B_{2g}, A_{1g}, E_g, and B_{1g} modes obtained from experiments on bulk RuO_2 is 87 meV, 80 meV, 65 meV, and 20 meV, respectively [1]. Note that the frequencies of the E_g and

A_{1g} modes of TiO_2, which are 55 meV and 76 meV respectively, are close to the frequencies of these corresponding modes in RuO_2.

	532 nm			455 nm		
Mode	(001)	(101)	(110)	(001)	(101)	(110)
B_{2g}	87	87	87	87	86	87
A_{1g}	79	79	79	78	78	79
E_g	64	64	65	64	63	65
B_{1g}	-	-	-	20	21	20

TABLE S4. Frequency of Raman modes in meV measured at room temperature using 532 nm and 455 nm excitation in RuO_2 grown on (001), (110) and (101) TiO_2 substrates. The B_{1g} mode was not detected using 532 nm excitation.

We resolved the B_{1g} mode of RuO_2 in our experiments using 455 nm excitation (illustrated in Fig. S2(a) below). The frequencies of the Raman modes of RuO_2 are near identical (differing by less than 1 meV) using the two excitation wavelengths.

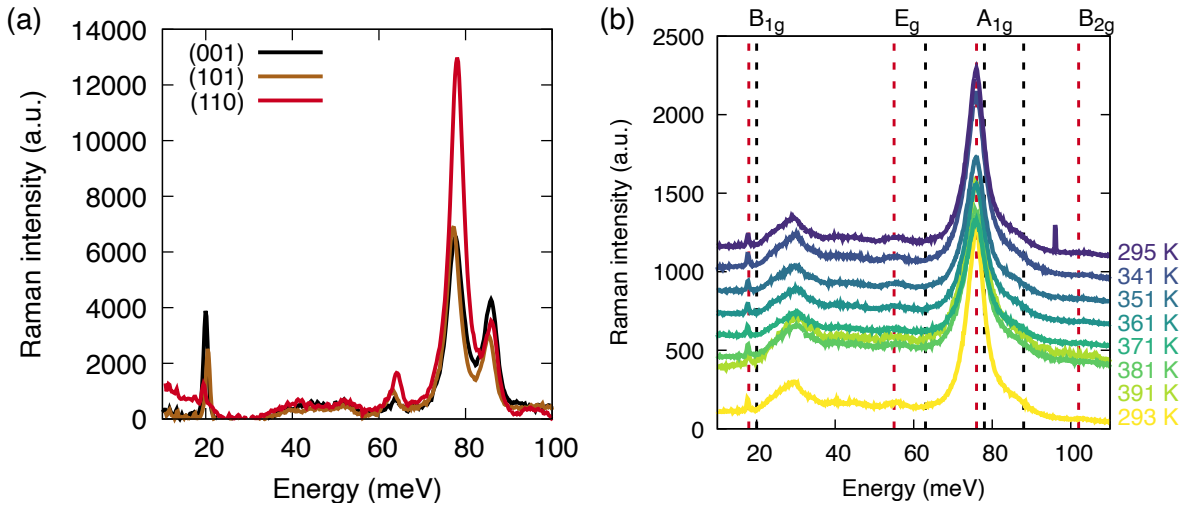

FIG. S2. (a) Raman spectra obtained at 455 nm excitation for RuO_2 films grown on TiO_2 (001), (101) and (110) substrates. (b) Temperature dependent Raman spectra of 40 nm thick RuO_2 grown on TiO_2 measured at 532 nm excitation. The red dotted lines mark the position of the TiO_2 Raman modes while the black dotted lines are the RuO_2 Raman modes measured in our 155 nm thick films.

The results in the main text use RuO_2 films that are 155 nm. We also consider the effect that a lower film thickness has on the vibrational properties of RuO_2 by measuring the temperature dependent Raman spectra of 40 nm RuO_2 films. The results are illustrated in Fig. S2(b). One challenge with identifying the Raman modes of RuO_2 in this spectra is the large contribution from the TiO_2 substrate. Notably the A_{1g} mode of TiO_2 which is at ∼75 meV nearly coincides with the A_{1g} mode of RuO_2. In addition to the A_{1g} mode of TiO_2 which has the largest intensity in the measurements on the 40 nm thick RuO_2 heterostructure, the B_{1g} of TiO_2 at ∼ 17 meV also coincides with the RuO_2 B_{1g} mode. The peak that is centered at ∼30 meV in Fig. S2(b) is likely due to second-order Raman processes in the TiO_2 substrate.

In Figure S3 below we illustrate the optical transmittance measured in the RuO_2 grown on TiO_2. Note that for each film there is a pronounced peak in the transmission at ∼2 eV, which coincides with the reduction in the reflectivity (see main text) that occurs at the same energy.

For the reflectivity calculations reported in the main text we use a Drude term of 0.2 eV to set the imaginary component of the plasma frequency. In Figure S4 below we illustrate the dependence of the calculated reflectivity on the choice of the Drude term where we vary it from 0.02 eV to 0.5 eV. Note that for the region of energies that we perform our measurements (∼ 1 eV to ∼ 3 eV) the reflectivity is relatively independent of the choice in the Drude

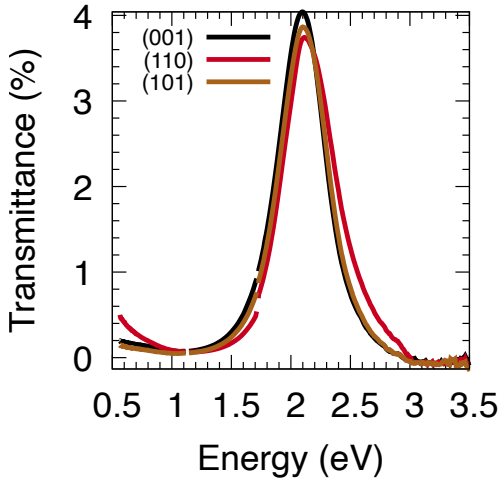

FIG. S3. Optical transmittance measured on RuO_2 films grown on TiO_2 (001), (101) and (110) substrates.

term.

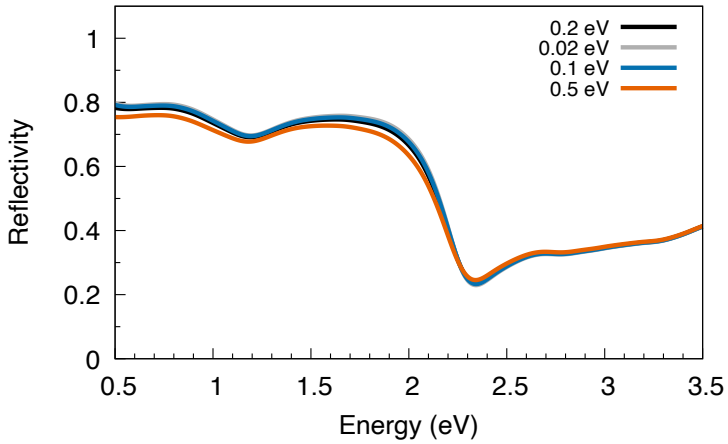

FIG. S4. Dependence of Drude term on the real part of the refractive index

V. EFFECT OF SPIN-ORBIT COUPLING AND ALTERMAGNETISM ON THE ELECTRONIC STRUCTURE OF RuO_2

The optical properties of RuO_2 in the main text are calculated without the inclusion of spin-orbit coupling. Since Ru and O are both light elements we expect the effect of spin-orbit splitting on the electronic structure to be weak. To confirm this we compare the non-magnetic electronic structure and optical reflectivity of RuO_2 with and without spin-orbit coupling in Fig. S5 below.

VI. r^2SCAN CALCULATIONS

For the calculations in the main text we use the GGA and GGA+U functional to assess the impact of nonmagnetic versus magnetic order on the properties of RuO_2. Below we explore whether a meta-GGA functional, specifically the r^2SCAN functional with nonmagnetic versus altermagnetic order leads to discernable differences in the density of states at the Fermi level, $N(E_F)$, the plasma frequency and vibrational frequencies. This comparison along with our nonmagnetic calculations using GGA and the results from experiment (Table 1 of the main text) are listed in

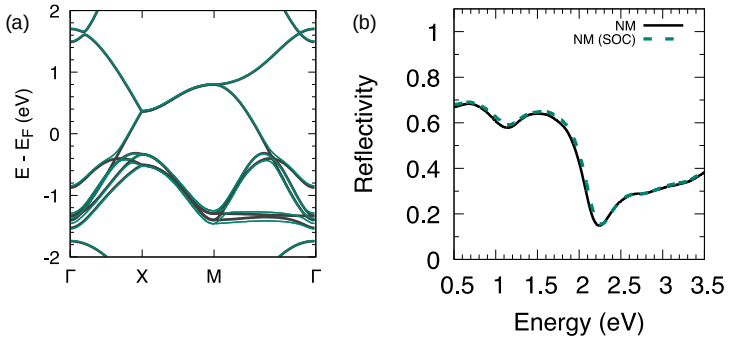

FIG. S5. Comparison of the non-magnetic RuO_2 electronic structure and optical properties with (green) and without (grey) spin-orbit coupling. (a) Band structure and (b) optical reflectivity.

Table S5 below. Consistent with our findings in the main text we also find nonmagnetic r^2SCAN calculations lead to properties of RuO_2 that are closer to experiment.

	NM (GGA)	NM (r^2SCAN)	AM r^2SCAN	Experiment
Density of states (states eV^{-1} Ru^{-1} $spin^{-1}$)				
$N(E_F)$	0.99	0.79	0.78	1.10
Plasma frequencies (eV)				
ω_x	3.21	3.09	2.72	3.16
ω_z	3.40	3.28	2.62	3.34
Raman frequencies (meV)				
B_{2g}	88	88	89	87
A_{1g}	78	78	83	80
E_g	63	64	65	65
B_{1g}	20	19	21	20

TABLE S5. Comparison of the density of states at the Fermi level, $N(E_F)$, plasma frequencies (ω) and the frequencies of the Raman modes of bulk RuO_2 computed with GGA and r^2SCAN in the nonmagnetic (NM) and altermagnetic (AM) state. We compare to experimental results with the values reported in Table 1 in the main text.

VII. EFFECT OF RU VACANCIES ON THE ELECTRONIC PROPERTIES OF RUO_2

In the main text we consider the role of hole doping on the optical properties of RuO_2, motivated by the prediction that hole doping may lead to altermagnetic order in RuO_2 [2]. Ru vacancies have been invoked as a possible source of hole doping [2]. To assess whether this is plausible we conducted supercell calculations of Ru vacancies in RuO_2 for three different Ru vacancy concentrations, 1.4%, 4.2%, and 6.2%. For each of these calculations we calculate the position of the Fermi level and compare to the Fermi level position in the pristine supercell. We find the Fermi level shifts to lower energies as a function of increasing Ru vacancy concentration as illustrated in Figure S6, consistent with these vacancies acting as a potential source of hole doping. For the largest Ru vacancy concentration that we consider when the magnetically ordered state is the ground state we find localized moments on the Ru ions that are

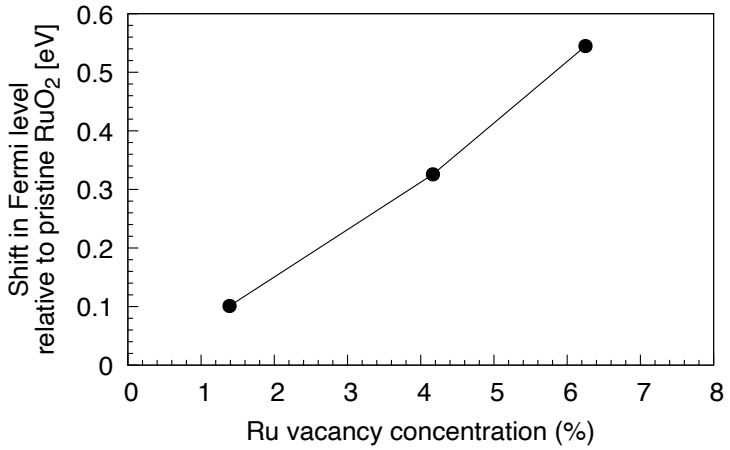

FIG. S6. Shift in the Fermi level with respect to pristine RuO_2 as a function of Ru vacancy concentration obtained using supercell calculations at the GGA level of theory.

second nearest-neighbor to the vacancy site with a moment of $\sim$0.3 μ_B.

[1] S. Rosenblum, W. Weber, and B. Chamberland, Phys. Rev. B **56**, 529 (1997).
[2] A. Smolyanyuk, I. I. Mazin, L. Garcia-Gassull, and R. Valentí, Phys. Rev. B **109**, 134424 (2024).